Optimal wave focusing in elastic media

Farhad Bazargani and Roel Snieder
Center for Wave Phenomena, Colorado School of Mines, Golden, CO 80401, USA

ABSTRACT
Time-reversal (TR) methods provide a simple and robust solution to source imaging problems. However, for recovering a well resolved image of the source, TR requires a balanced illumination of the target from all angles. When acquisition is incomplete and a balanced illumination is not possible, the TR solution may not be adequate. In a previous paper, by formulating source imaging as an optimization problem, we presented a method named Backus-Gilbert focusing (BG) to enhance the performance of time-reversal focusing in acoustic media despite incomplete acquisition. Here, we generalize the theory of Backus-Gilbert focusing for application in elastic media.

Key words: elastic waves, source imaging, focusing, optimization, time-reversal, microseismic

1 INTRODUCTION

Since the beginning of modern seismology, understanding earthquake sources has been a focus of research. Source parameters such as time, location, focal mechanism, and rupture process provide invaluable insight for understanding fault systems and earthquakes. Exploration seismologists study microseismic events to acquire information about the inducing mechanism and the size and orientation of fractures in a hydrofracturing experiment (Rentsch et al., 2007; Baig and Urbancic, 2010; Maxwell and Urbancic, 2001; Eaton and Forouhideh, 2011).

Conventional methods for studying seismic sources rely on the kinematic information in seismic data to invert for the source parameters (Stein and Wysession, 2003) . More recently, inversion methods based on full-waveform data aim at solving for the moment tensors that completely describe the focal mechanism of the seismic source (Jost and Herrmann, 1989; Baig and Urbancic, 2010; Song and Toksöz, 2011). The stability of these full waveform inversion methods is limited by the acquisition geometry and the level of noise in data (Song and Toksöz, 2011; Eaton and Forouhideh, 2011). In particular the solid angle subtended by the receiver array, as viewed from the source location, plays a fundamental role in the stability of the inversion; the smaller solid angles imply less stability (Eaton and Forouhideh, 2011).

An alternative approach to studying seismic sources is through direct imaging of the source using TR focusing methods, which are based on TR invariance of the wave operator (Fink, 1997, 2006, 2008; Larmat et al., 2006). TR based techniques are routinely used for seismic event location and source imaging (Larmat et al., 2010). The effectiveness of TR source imaging techniques is also reduced by incomplete acquisition because to resolve the source, TR requires a well-balanced illumination of the target.

To compensate for the adverse effects of incomplete acquisition on TR, Bazargani et al. (2014) presented a new method, named Backus-Gilbert focusing, in which source imaging in acoustic media is formulated as an optimization problem. The only prerequisites of the method are knowledge of the acoustic medium and an estimate of the source location. In this paper, we generalize the theory of the BG focusing for elastic media.

The organization of the paper is as follows: We first lay out the theoretical foundation of our new approach to wave focusing and show how to design waveforms to optimally image a point source with unknown parameters using sparse data (section 2). Next, in section 3, we discuss how BG is connected to TR focusing and show that TR can be regarded as a special case of the more general solution to wave focusing that BG provides. Section 4 is devoted to a numerical example where we apply the elastic BG method in imaging a double-couple point source. In section 5 we discuss various aspects of the BG method and elaborate further on some explicit and implicit assumptions that are used in the construction of the new approach and their significance. In appendix A, we show that the theory of the method presented

in section 2 is equally applicable to spatio-temporally extended sources.

2 OPTIMIZED IMAGING OF A POINT SOURCE

2.1 Notation

Before delving into the details of the BG optimization for elastic source imaging, we define notational conventions that are used throughout this paper.
1. We use Einstein's notational convention for repeated indices: whenever an index (a subscript or a superscript) is repeated, summation over that index is implied.
2. All superscripts are associated with the receivers and take any integer value between 1 and N.
3. All subscripts denote spatial components.
4. Fourier transforms follow the convention

$$f(\mathbf{x},\omega) = \int f(\mathbf{x},t)\, e^{i\omega t}\, dt.$$

5. A Green tensor is 3×3 in $3D$ and is 2×2 in $2D$ with elements $\mathbf{G}_{np}(\mathbf{x}^i, t; \boldsymbol{\xi}, 0)$ denoting the value of the n^{th} component of the displacement field measured at $\mathbf{x} = \mathbf{x}^i$ and time t, where the displacement field is generated by a unidirectional unit impulse parallel to the p^{th} coordinate axis, applied at $\mathbf{x} = \boldsymbol{\xi}$ and $t = 0$.
6. As a superscript, the asterisk $*$ denotes complex conjugation, otherwise, it represents time convolution of two functions.

2.2 Formulation

Consider an elastic medium in which a single point source radiates seismic energy from an unknown location $\boldsymbol{\xi} \in W$, where W represents a subset of the medium that contains the source. (In practice, to determine the extent of W, a rough estimate of the source location $\boldsymbol{\xi}$ is required). We also assume that the source mechanism of the point source is described by an unknown moment tensor $\mathbf{M}(t)$ with an unknown time dependence.

Suppose that we sample the source displacement field $\mathbf{u}(\mathbf{x}, t)$ by N multicomponent receivers at locations $\mathbf{x}^i$. This is a passive experiment in the sense that all receivers start recording at time $t = 0$ and stop at $t = T$ such that T is large enough to allow adequate sampling of the source displacement field $\mathbf{u}(\mathbf{x}, t)$.

Let us denote the n^{th} component of the data vector $\mathbf{d}(t)$ recorded by the station at $\mathbf{x}^i$ by d_n^i. As shown by Aki and Richards (2002), this data can be expressed as

$$d_n^i(t) = \mathbf{u}_n(\mathbf{x}^i, t) = M_{pq}(t) * \frac{\partial G_{np}(\mathbf{x}^i, t; \boldsymbol{\xi}, 0)}{\partial x_q}, \qquad (1)$$

where M_{pq} denotes the elements of the source moment tensor $\mathbf{M}$, and G_{np} represents the elements of the elastodynamic Green tensor $\mathbf{G}$. In the frequency domain, equation 1 becomes

$$d_n^i(\omega) = M_{pq}(\omega)\, \frac{\partial G_{np}(\mathbf{x}^i; \boldsymbol{\xi}, \omega)}{\partial \xi_q}. \qquad (2)$$

The body force equivalent of our point source can be written as (Aki and Richards, 2002)

$$f_n(\mathbf{x}, t) = -M_{nq}(t)\, \frac{\partial \delta(\mathbf{x} - \boldsymbol{\xi})}{\partial x_q}, \qquad (3)$$

where δ represents the Dirac delta function. Having defined the configuration of the experiment, the data, and the body force equivalent of the point source, we are ready to formulate the optimization problem.

According to the time-reversal process, after recording the data $\mathbf{d}(t)$ associated with a source, a time-reversed version of the source wavefield $\mathbf{u}(\mathbf{x}, T - t)$ can be reconstructed by broadcasting time-reversed data $\mathbf{d}(T - t)$ from each receiver. This process works well when the acquisition geometry of the experiment is complete and allows for adequate sampling of the source wavefield. However, with incomplete acquisition, the TR process cannot properly reconstruct the time-reversed source displacement field. Therefore, the simple process of time-reversing the data and re-injecting them is suboptimal in such situations.

Our goal is to find signals $a_n^i(t)$, for each component of each receiver, such that upon injection and propagation from the receivers, the resulting displacement field $\boldsymbol{\psi}(\mathbf{x}, t)$ correctly reconstructs the time-reversed source displacement field $\mathbf{u}(\mathbf{x}, T - t)$. To accomplish this goal, we define an objective function

$$J = \iint_W |\boldsymbol{\psi}(\mathbf{x}, t) - \mathbf{u}(\mathbf{x}, T - t)|^2\, d\mathbf{x}\, dt, \qquad (4)$$

where W denotes a subset of the medium that contains the source, $\mathbf{u}$ is the source displacement field, and $\boldsymbol{\psi}$ is the reconstructed displacement field with its components

$$\psi_n(\mathbf{x}, t) = G_{np}(\mathbf{x}, t; \mathbf{x}^i, 0) * a_p^i(t). \qquad (5)$$

We show in Appendix B that in the near-source region the particle displacements are proportional to the body force equivalent of the source. This makes intuitive sense because if a force is applied somewhere in an elastic medium then the particles pushed by the force are expected to move in the same direction as the force. Therefore, we can write

$$\mathbf{u}(\mathbf{x}, t) = C\, \mathbf{f}(\mathbf{x}, t), \qquad (6)$$

where C denotes a proportionality constant with dimensions of [displacement]/[force]. Here, for simplicity, we assume $C = 1$.

Using equations 3, 5, and 6, the objective function

4 is given by

$$J = \sum_{r}^{3} \int_W |G_{rp}(\mathbf{x}, t; \mathbf{x}^i, 0) * a_p^i(t) + M_{rq}(T-t)\, \frac{\partial \delta(\mathbf{x}-\boldsymbol{\xi})}{\partial x_q}|^2 \, d\mathbf{x}. \tag{7}$$

In the frequency domain, this objective function can be written as

$$J(\omega) = \sum_{r=1}^{3} \int_W |G_{rp}^i \, a_p^i + e^{i\omega T} \, M_{rq}^* \, \frac{\partial \delta(\mathbf{x}-\boldsymbol{\xi})}{\partial x_q}|^2 \, d\mathbf{x}, \tag{8}$$

where we have used the abbreviated notation $G_{rp}^i = G_{rp}(\mathbf{x}; \mathbf{x}^i, \omega)$, $a_p^i = a_p^i(\omega)$, and $M_{rq} = M_{rq}(\omega)$.

Objective function 8 must be minimized for each frequency independently. To this end, we differentiate $J(\omega)$ with respect to $a_m^{n^*}(\omega)$ for some particular m and n, and set $\partial J(\omega)/\partial a_m^{n*}(\omega) = 0$. This gives

$$\begin{aligned} a_p^i(\omega) \int_W G_{rm}^{n*} \, G_{rp}^i d\mathbf{x} \\ &= - \int_W e^{i\omega T} \, G_{pm}^{n*} \, M_{pq}^* \, \frac{\partial \delta(\mathbf{x}-\boldsymbol{\xi})}{\partial x_q} \, d\mathbf{x} \\ &= + \int_W e^{i\omega T} \, \delta(\mathbf{x}-\boldsymbol{\xi}) \, M_{pq}^* \, \frac{\partial G_{pm}^{n*}}{\partial x_q} \, d\mathbf{x} \\ &= e^{i\omega T} \, M_{pq}^* \, \frac{\partial G_{pm}^*(\boldsymbol{\xi}; \mathbf{x}^n, \omega)}{\partial x_q} \\ &= e^{i\omega T} \, M_{pq}^* \, \frac{\partial G_{mp}^*(\mathbf{x}^n; \boldsymbol{\xi}, \omega)}{\partial \xi_q} \, , \end{aligned} \tag{9}$$

where in the last three steps of equation 9, we used integration by parts, the sifting property of the delta function, and the reciprocity principle for the components of the Green function, respectively.

Next, in equation 9, we replace indices m with n, n with i, and i with j to get

$$a_p^j(\omega) \int_W G_{rn}^{i*} \, G_{rp}^j \, d\mathbf{x} = e^{i\omega T} \, M_{pq}^* \, \frac{\partial G_{np}^*(\mathbf{x}^i; \boldsymbol{\xi}, \omega)}{\partial \xi_q} \, . \tag{10}$$

Comparing the right hand side of 10 with that of 2, we can simplify equation 10 as

$$a_p^j(\omega) \int_W G_{rn}^{i*} \, G_{rp}^j \, d\mathbf{x} = e^{i\omega T} \, d_n^{i*}. \tag{11}$$

Equation 11 represents a linear system of equations that can be concisely expressed as

$$\boldsymbol{\Gamma}(\omega) \, \mathbf{a}(\omega) = e^{i\omega T} \, \mathbf{d}^*(\omega), \tag{12}$$

which must be independently solved for the vector $\mathbf{a}(\omega)$ for each frequency. More explicitly, equation 12 can be written (in $3D$) as

$$\underbrace{\begin{pmatrix} \boldsymbol{\Gamma_{11}} & \boldsymbol{\Gamma_{12}} & \boldsymbol{\Gamma_{13}} \\ \boldsymbol{\Gamma_{21}} & \boldsymbol{\Gamma_{22}} & \boldsymbol{\Gamma_{23}} \\ \boldsymbol{\Gamma_{31}} & \boldsymbol{\Gamma_{32}} & \boldsymbol{\Gamma_{33}} \end{pmatrix}}_{\boldsymbol{\Gamma}}^{3N\times 3N} \underbrace{\begin{pmatrix} \mathbf{a}_1 \\ \mathbf{a}_2 \\ \mathbf{a}_3 \end{pmatrix}}_{\mathbf{a}}^{3N\times 1} = e^{i\omega T} \underbrace{\begin{pmatrix} \mathbf{d}_1 \\ \mathbf{d}_2 \\ \mathbf{d}_3 \end{pmatrix}^*}_{\mathbf{d}^*}^{3N\times 1}, \tag{13}$$

in which the $3N \times 3N$ matrix $\boldsymbol{\Gamma}$ consists of nine $N \times N$ submatrices $\boldsymbol{\Gamma}_{kl}$ defined as

$$\Gamma_{kl}^{ij} = \int_W G_{rk}^{i*} \, G_{rl}^j \, d\mathbf{x} \, , \tag{14}$$

the $3N \times 1$ vector $\mathbf{a}$ contains three $N \times 1$ subvectors corresponding to the three components of the optimized signals

$$\mathbf{a}_k = \begin{pmatrix} a_k^1 \\ a_k^2 \\ . \\ . \\ a_k^N \end{pmatrix}, \tag{15}$$

and the $3N \times 1$ vector $\mathbf{d}$ contains three $N \times 1$ subvectors corresponding to the three components of the recorded data

$$\mathbf{d}_k = \begin{pmatrix} d_k^1 \\ d_k^2 \\ . \\ . \\ d_k^N \end{pmatrix}. \tag{16}$$

Note that in equation 14, a summation is carried out over the index r.

The significance of equation 12 is that $\boldsymbol{\Gamma}$ on the left hand side of equation 12 can be computed (based on equation 14) as long as the medium is known and an estimate of the source location is available. The right hand side of equation 12 depends only on the recorded data, meaning that all the information the method requires about the unknown source is available and encoded within the data. Therefore, equation 12 can be solved for $\mathbf{a}(\omega)$.

Even if only a subset of the data components are available, the formalism presented above is still valid and applicable. This is because equation 13 can be readily modified to form a new system that corresponds to the available data components. As a simple example, equation 13 can be modified for application in $2D$ as

$$\underbrace{\begin{pmatrix} \boldsymbol{\Gamma_{11}} & \boldsymbol{\Gamma_{12}} \\ \boldsymbol{\Gamma_{21}} & \boldsymbol{\Gamma_{22}} \end{pmatrix}}_{\boldsymbol{\Gamma}}^{2N\times 2N} \underbrace{\begin{pmatrix} \mathbf{a}_1 \\ \mathbf{a}_2 \end{pmatrix}}_{\mathbf{a}}^{2N\times 1} = e^{i\omega T} \underbrace{\begin{pmatrix} \mathbf{d}_1 \\ \mathbf{d}_2 \end{pmatrix}^*}_{\mathbf{d}^*}^{2N\times 1}, \tag{17}$$

where $\boldsymbol{\Gamma}_{kl}$, $\mathbf{a}_k$ and $\mathbf{d}_k$ are defined by equations 14, 15, and 16, respectively. Similarly, equation 13 can be modified for $3D$ cases where only a subset of data (e.g., only vertical components) is available for all or some receivers,.

After solving equation 12 and finding $\mathbf{a}(\omega)$ for all frequencies, we can compute the optimal time-domain signals $\mathbf{a}^i(t)$. To image the source, these optimized signals must be injected and propagated by the receivers and the resulting wavefield $\boldsymbol{\psi}(\mathbf{x}, t)$ must be scanned for the image of the source.

We showed in this section that we can approach the problem of imaging an unknown point source as an optimization problem. We started our argument by assuming that there is only one point source inside the medium. However, as we show in appendix B, this argument can be generalized to hold true for any arbitrary distributed source. This is because a distributed source can be regarded as a collection of point sources. In other words, equation 12 can be used to find the optimal signals for imaging any type of source regardless of it being a point source or not.

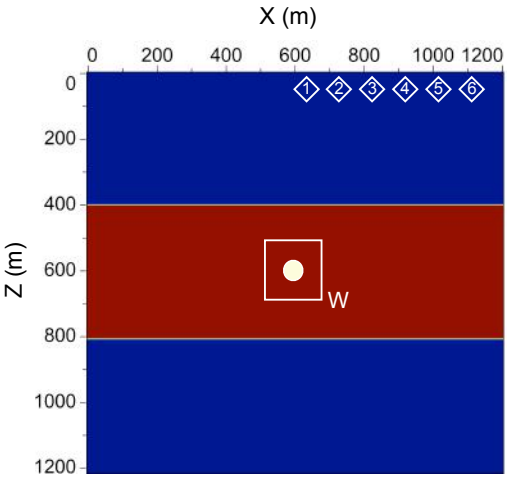

Figure 1. The elastic model and the configuration of the numerical experiment of section 4. The white diamonds show the location of the stations, the white square W depicts a small subset of the medium that contains the focusing target which is represented by the white circle. The blue background color represents $v_p = 3000\ m/s$, $v_s = 2000\ m/s$, and $\rho = 2000\ kg/m^3$. The red background color represents $v_p = 3750\ m/s$, $v_s = 2500\ m/s$, and $\rho = 3000\ kg/m^3$.

3 CONNECTION WITH TIME REVERSAL

The Backus-Gilbert focusing method (BG), introduced in section 2, provides a more general solution to the wave-focusing problem compared to TR. In fact, there is a close mathematical relationship between these methods. To be able to see the connection between BG and TR, we discuss the structure of $\boldsymbol{\Gamma}$ and examine the significance of its 9 submatrices (shown in equation 13) to develop a better understanding of their function in the optimization process.

All elements of $\boldsymbol{\Gamma}$ hold crucial information about the configuration of the focusing experiment, i.e., the relative positions of the stations with respect to the inhomogeneities in the propagation medium and the focusing target. The role of the submatrix $\boldsymbol{\Gamma}_{kl}$ can be described as determining how the signal injected by the k^{th} component of each receiver must be adjusted with respect to the signals emitted by the l^{th} components of the other receivers in order to optimally reconstruct the source displacement field.

For example, the diagonal submatrix $\boldsymbol{\Gamma}_{11}$ adjusts the signal emitted by the 1^{st} component of each receiver with respect to the 1^{st} signal injected by other receivers. In contrast, the off-diagonal submatrix $\boldsymbol{\Gamma}_{32}$ is responsible for adjusting the signals emitted by the 3^{rd} component of each receiver with respect to signals emitted by the 2^{nd} component of the other receivers.

A quick inspection of equation 14 reveals that $\boldsymbol{\Gamma}$ is, by definition, a Hermitian matrix; this means that for the submatrices of $\boldsymbol{\Gamma}$, we have $\boldsymbol{\Gamma}^{ij}_{kl} = \boldsymbol{\Gamma}^{ji\,*}_{lk}$. Therefore, whatever function or role we attribute to $\boldsymbol{\Gamma}_{kl}$, the same function can be assumed for its conjugate transpose submatrix $\boldsymbol{\Gamma}_{lk}$.

With this background about the anatomy of $\boldsymbol{\Gamma}$, we are now ready to study the relationship between BG and TR. Let us approximate $\boldsymbol{\Gamma}$ in equation 12 by the identity matrix I to get

$$\mathbf{a}(\omega) = e^{i\omega T}\mathbf{d}^*(\omega). \tag{18}$$

The complex conjugation and multiplication of $\mathbf{d}(\omega)$ in equation 18 by $e^{i\omega T}$ for all frequencies amounts to in-place time-reversal of the data $\mathbf{d}(t)$ in the time domain. In other words, using the identity matrix as the most simplistic approximation for $\boldsymbol{\Gamma}$ in equation 12 results in a new system of equations (as in equation 18) which describes exactly the same process as time-reversal. By replacing $\boldsymbol{\Gamma}$ with the identity matrix, we turn off the function of the submatrices of $\boldsymbol{\Gamma}$. This amounts to ignoring the cross-talk between the components of the stations and make them work independently from the other stations to inject the time-reversed data. Therefore, we might say that TR is a special cases of the more-general BG with a crude approximation of $\boldsymbol{\Gamma}$ as the identity matrix.

4 NUMERICAL EXPERIMENT

We apply the elastic BG method in a 2D numerical experiment to image a point source with a double-couple mechanism and compare the result with the same image produced by TR. The configuration of the experiment is shown in Figure 1. The six diamonds represent the receivers, the white circle depicts the source location, and the white square shows the optimization window W, used in the definition of the objective function in equa-

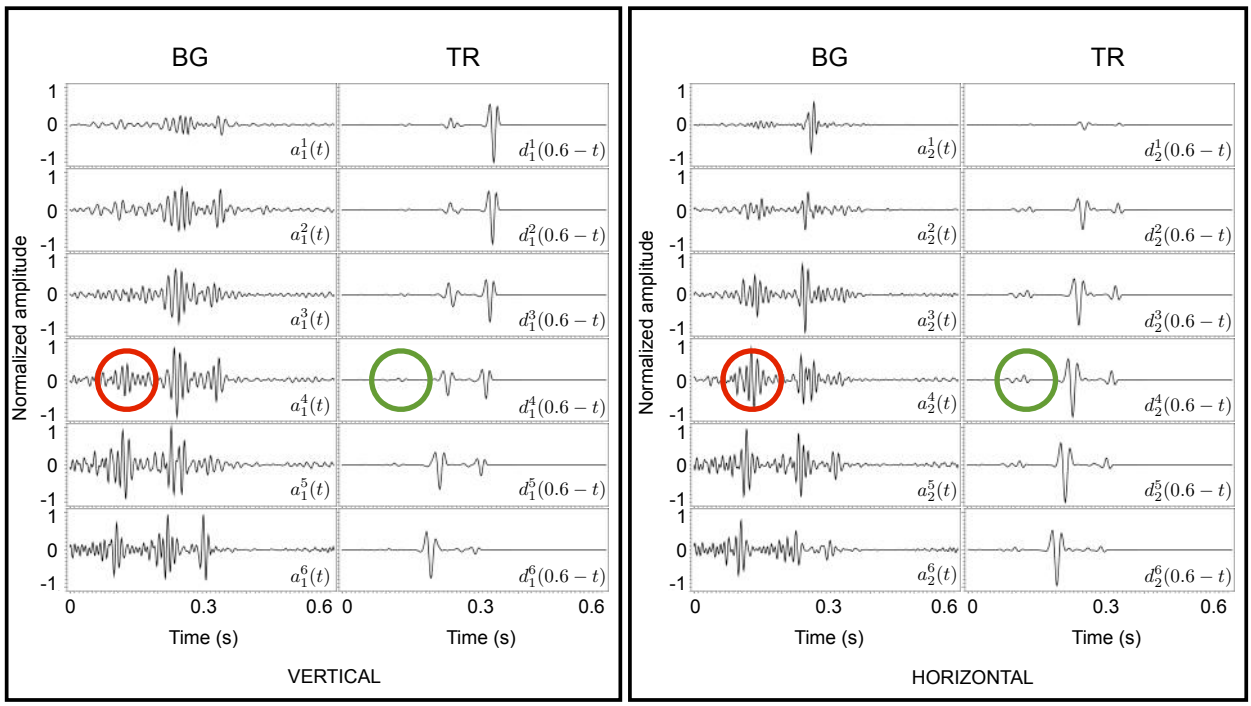

Figure 2. Vertical component of the optimal signals versus the timer-reversed vertical component of the data (left panel), and horizontal component of the optimal signals versus the timer-reversed horizontal component of the data (right panel). The weak reflection energies (green circles) are amplified in the optimize traces (red circles).

tion 4. The earth model used for the wave propagation is a heterogeneous elastic 2D model (Figure 1) consisting of three layers. Wave propagation is simulated using an explicit finite-difference approximation of the 2D elastic isotropic wave equation with an absorbing boundary condition.

The data $\mathbf{d}^i(t)$ is generated by a horizontal point source of slip with a double-couple mechanism located at $\boldsymbol{\xi} = (600\,m, 600\,m)$ within W. The time dependence of the source is given by a Ricker wavelet with peak frequency of $55Hz$ and peak time $t = 100ms$. We sample the displacement field generated by this source using receivers at $\mathbf{x}^i$ for $T = 0.6\,s$. After simulating the data, for the rest of the experiment, we pretend that we do not know the actual location and time of the source.

To form the Gram matrix $\boldsymbol{\Gamma}$, in equation 17, we require the Green functions $G(\mathbf{x}, t; \mathbf{x}^i, 0)$. We approximate these Green functions by injecting a band limited spike with frequencies between $2\,Hz$ and $140\,Hz$ at each receiver location $\mathbf{x}^i$ and propagating the wavefield for $T = 0.6\,s$. These wavefields are then Fourier transformed to the frequency domain and used in equation 14 to compute the elements of the 12×12 matrix $\boldsymbol{\Gamma}$ independently for all frequencies within the bandwidth of the experiment. In computing the integral of equation 14 over W, the oscillatory integrand is tapered near the edges of integration window W to avoid dominant contribution from the end points.

At this point, we can form the system of equations 17 for each frequency independently and solve the system for $\mathbf{a}^i(\omega)$, the Fourier coefficients of the optimized signals $\mathbf{a}^i(t)$. These optimized signals are then broadcast by the receivers to generate the optimal displacement field $\boldsymbol{\psi}(\mathbf{x}, t)$ that will focus at the correct source location. Note that, in this $2D$ example,$\boldsymbol{\psi}(\mathbf{x}, t)$ is a vector field with 2 components, a vertical and a horizontal component.

The last step is to scan this optimal wavefield to detect and extract the source image which has been created at location $\boldsymbol{\xi} \in W$ and at the correct time associated with the source activation time. After detecting the source image, the actual source location, time, and the spatio-temporal characteristics of the source can be inferred from that image.

Possible criteria to detect the source image can include high energy or a particular type of radiation pattern which is expected for the source. For example, a seismic source with a double-couple mechanism has characteristic four-lobe radiation patterns for the radial and transverse displacement components (Aki and Richards, 2002). The radial and transverse components of the displacement field can be readily computed as

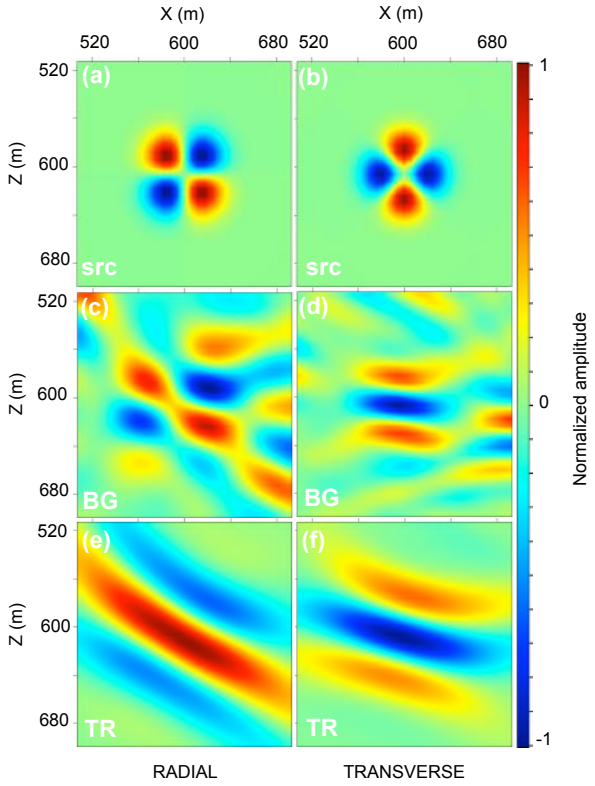

Figure 3. Radial (a) and transverse (b) components of the source displacement field enclosed within W at the activation time of the source are compared with the P-wave (c) and S-wave (d) images of the source produced by BG, and with the P-wave (e) and S-wave (f) images of the source produced by TR.

the curl and divergence of the displacement field, respectively.

Figures 2 and 3 summarize the results of the numerical experiment described above. Figure 2 consists two panels. The left panel depicts the vertical component of the optimal signals in the column labeled BG, and the vertical component of the time-reversed data in the column labeled TR. Similarly, the right panel depicts the horizontal component of the optimal signals in the column labeled BG, and the horizontal component of the time-reversed data in the column labeled TR. The signals in each column (of both panels) have been normalized by dividing all samples by the maximum absolute value of the amplitude of all traces in the same column.

The optimization process has produced signals that are different from their corresponding time-reversed data in both amplitude and shape. For example, the small amplitude events in the time-reversed traces (e.g., the energy encircled in green) correspond to the reflection energy that is reflected from the discontinuity at $Z = 800\,m$ in Figure 1. Note how the same reflected events (e.g. the energy encircled in red) are amplified by BG in the optimally computed signals.

Figures 3a and 3b show the P- and S-wave snapshots of the wavefield generated by the horizontal dislocation source in this experiment. More specifically, Figures 3a and 3b depict the portion of the divergence (radial component) and curl (transverse component) of the source displacement field enclosed within W at the activation time of the double-couple point source. We can think of Figure 3a as the exact P-wave image and of Figure 3b as the exact S-wave image of the source. The radial and transverse component of the optimally reconstructed source displacement field $\boldsymbol{\psi}(\mathbf{x}, t)$ at the time of focus are shown in Figure 3c and Figure 3d. These are the P- and S-wave images of the source obtained by taking the divergence and curl, respectively, of $\boldsymbol{\psi}(\mathbf{x}, t)$. Finally, the P- and S-wave images of the source produced by TR are depicted in Figures 3e and 3f, respectively.

The BG images (second row of Figure 3) are superior to the TR images (third row) in many aspects. For example, note how the four lobes of the P-wave radiation pattern are resolved by BG in Figure 3c, whereas it is impossible to recognize them in the corresponding TR image in Figure 3e. The four-lobe S-wave radiation pattern is not resolved by either BG or TR. Nevertheless, compared to the TR image (3f), the BG image (3d) resembles the exact S-wave image (3b) more closely in both size and orientation.

The improvement of the resolution in the BG images, can be attributed to a more balanced illumination of the target. This is made possible by using the amplified reflected events in the optimized signals shown in Figure 2. When the optimized signals are propagated, a strong coherent burst of energy is create by these amplified events. This coherent energy travels in advance and part of it, after bouncing off the reflector at $Z = 800\,m$, illuminates the target from underneath. Of course, BG did not create this energy out of nowhere. The energy is also present in the TR experiment, but it is much weaker. All that is done by BG was to detect this weak energy and amplify it in order to balance the target illumination. Effectively, this is equivalent of using the reflector at $Z = 800\,m$ as an elastic mirror in order to augment the illumination angles, which in the case of TR are limited to the small angle subtended by the first and the last receivers.

5 DISCUSSION

In the formulation of the elastic BG method in section 2 several assumptions were made. The most important of these assumptions is knowledge of the elastic medium (e.g. P- and S-wave velocities and density). This is because an accurate model for the medium is vital for computing the Green tensor for each receiver location and the Green tensors are needed for computing the $\mathbf{\Gamma}$ matrix.

Knowledge of the medium is essential to any source imaging method. In general, using an inaccurate velocity model degrades the image quality or causes the image of the source to be created at a wrong time or location. BG focusing is not an exception in this respect. For instance, in the example shown in section 4, BG relies on amplifying the weak reflection energy in data in order to compensate for the incomplete acquisition. In this case, to effectively balance the illumination, BG requires an accurate velocity model that contains the reflectors that are associated with the reflection energy recorded in the data. Otherwise, BG will not be as effective as it is portrayed by the example in section 4 and, depending on the fidelity of the velocity model in predicting the reflections and its accuracy, the BG image of the source may be degraded and approach that of TR. In short, because TR works based on the crude approximation $\mathbf{\Gamma} \approx \mathbf{I}$, when an accurate model is available, TR is not as effective as BG. However, TR is less sensitive to inaccuracies in the model and is more robust than BG in tolerating errors in the model.

Apart from the velocity model, we also need an estimate of the source location such that we can be certain that the source is somewhere within a limited area W. In practice, such an estimate is usually available. For instance, in earthquake semiology, the approximate location of the source is commonly calculated using common source location techniques that work based on kinematic information in data (Stein and Wysession, 2003). Similarly, in hydraulic fracturing monitoring surveys, geophysicist often have a good estimate of the size of the affected area around the injection well where microseismic energy is most likely to originate. The size of W is an important factor in determining the effectiveness of BG as a source imaging method. This is because W is used directly in the definition of the objective function 4 upon which we based the formulation of the BG method. With a limited number of receivers, the smaller W (the smaller the uncertainty in the location of the source) is, the easier it is to minimize the BG objective function. However, there is a lower limit on how small W can be to obtain best focusing results. Based on our tests (not shown here) the optimum focusing is achieved when the size of W is 2 to 3 times the dominant wavelength in the data.

The presence of noise in recorded data is an important matter that needs careful attention when applying BG to source imaging. In our numerical example of section 4, we did not include noise. Applying the BG method for source imaging depends on the validity of equation 12 which allows us to solve for optimal signals without explicit knowledge of the source parameters. However, in a real source imaging scenario, equation 12 does not hold exactly because recorded data always contain noise. Therefore, equation 12 must be replaced by

$$\mathbf{\Gamma}(\omega)\mathbf{a}(\omega) \approx e^{i\omega T}(\mathbf{d}^*(\omega) + \boldsymbol{\eta}^*(\omega)), \tag{19}$$

where $\boldsymbol{\eta}$ denotes the noise vector and $\mathbf{d}$ the theoretical noise-free data described by equation 2.

The stability of the solution $\mathbf{a}$ in equation 19 depends on the condition number of $\mathbf{\Gamma}(\omega)$, which itself depends on the configuration of the receivers, the properties of the medium, and the frequency ω for which $\mathbf{\Gamma}(\omega)$ is computed. If $\mathbf{\Gamma}(\omega)$ is ill-conditioned, then some regularization technique, e.g., truncated singular value decomposition (TSVD) can be used to find a stable solution to equation 19.

Computing $\mathbf{\Gamma}$ requires simulating the wave propagation to model the Green tensor for each receiver location. However, for a fixed configuration of receivers, $\mathbf{\Gamma}$ and its inverse have to be computed only once. (Recall that $\mathbf{\Gamma}$ on the left hand side of equation 12 depends only on the receiver geometry and the properties of the medium and the right hand side depends only on the recorded data.) Therefore, once $\mathbf{\Gamma}^{-1}$ is computed and stored, we can reuse it to solve equation 12 whenever a new source occurs. This means that for receivers with a fixed geometry, using BG to image multiple sources can be computationally very efficient.

6 CONCLUSION

Time-reversal (TR) focusing methods rely on the time-reversal invariance of the wave operator. When acquisition is incomplete, source imaging techniques based on time-reversal focusing are not optimal. In this paper, to overcome the limitations imposed by incomplete acquisition, we approach source imaging in elastic media as an optimization problem. The new approach, named Backus-Gilbert focusing (BG), provides a more general solution to elastic wave focusing than TR does.

To apply BG in source imaging, the medium must be known and also an estimate of the source position must be available. Apart from these two requirements, no other a priori information is needed by the method. Of course, since the method is formulated as an inverse problem that relies on the knowledge of the medium, it is more sensitive than TR to inaccuracies in the model. We showed with a numerical example simulating an elastic source imaging experiment with sparse receiver geometry, that BG can produce better resolved images of an unknown source than TR. For source imaging using receiver stations with a fixed geometry, the application of the method can be computationally efficient.

The presence of noise in data is an important issue that needs to be addressed by applying proper regularization. A high level of noise in data, depending on the condition number of the inverse problem, can compromise the effectiveness of BG.

One area of geophysics that is a good candidate for

application of BG is imaging earthquake sources. This is because of three reasons: The first reason is that a relatively reliable elastic model of the earth is available in global seismology which can be used by BG. The second reason is that the advantages of BG over TR are most pronounced in experiments with sparse (incomplete) acquisition geometry. The global network of seismometers does not have a uniform distribution on the Earth and therefore earthquakes that occur in certain areas cannot be recorded properly. And the third reason is that the data quality in terms of signal-to-noise ratio for the strong earthquakes recorded in global seismology are often very good.

7 ACKNOWLEDGMENTS

This research was supported by the sponsor companies of the Consortium Project on Seismic Inverse Methods for Complex Structures. We are thankful to Dr. Jon Sheiman for supporting us with invaluable insights. The software used to produce the results in the paper was written in Java and Jython with the use of libraries in the Mines Java Toolkit freely available at https://github.com/dhale/jtk.

REFERENCES

Aki, K., and P. Richards, 2002, Quantitative seismology 2nd edition: University Science Books.

Baig, A., and T. Urbancic, 2010, Microseismic moment tensors: A path to understanding frac growth: The Leading Edge, **29**, 320–324.

Bazargani, F., R. Snieder, and J. Sheiman, 2014, Optimal wave focusing in acoustic media: Technical Report CWP-791, Center for Wave Phenomena, Colorado School of Mines.

Eaton, D. W., and F. Forouhideh, 2011, Solid angles and the impact of receiver-array geometry on microseismic moment-tensor inversion: Geophysics, **76**, no. 6, WC77–WC85.

Fink, M., 1997, Time-reversed acoustics: Physics Today, **50**, no. 3, 30–34.

———, 2006, Time-reversal acoustics in complex environments: Geophysics, **71**, 151–164.

———, 2008, Time-reversal waves and super resolution: Journal of Physics:Conference Series, **124**, 1–29.

Jost, J. M., and R. Herrmann, 1989, A student's guide to and review of moment tensors: Seismological Research Letters, **60**, 37–57.

Larmat, C., R. A. Guyer, and P. A. Johnson, 2010, Time-reversal methods in geophysics: Physics Today, **63**, no. 8, 31–35.

Larmat, C., J. Montagner, M. Fink, and Y. Capdeville, 2006, Time-reversal imaging of seismic sources and application to the great sumatra earthquake: Geophysical Research Letters, **33**, L19312.

Maxwell, S. C., and T. I. Urbancic, 2001, The role of passive microseismic monitoring in the instrumented oil field: The Leading Edge, **20**, 636–640.

Rentsch, S., S. Buske, S. Luth, and A. Shapiro, 2007, Fast location of seismicity: A migration-type approach with application to hydraulic-fracturing data: Geophysics, **72**, S33–S40.

Song, F., and N. Toksöz, 2011, Full-waveform based complete moment tensor inversion and source parameter estimation from downhole microseismic data for hydrofracture monitoring: Geophysics, **76**, no. 6, WC103–WC116.

Stein, S., and M. Wysession, 2003, An introduction to seismology, earthquakes, and earth structure: Blackwell publishing.

Wu, R., and A. Ben-Menahem, 1985, The elastodynamic near field: Geophysical Journal of the Royal Astronomical Society, **81**, 609–621.

APPENDIX A: OPTIMIZED IMAGING OF AN EXTENDED ELASTIC SOURCE

In section 2, we formulated the BG optimization for imaging a point source. Here, we show that this formulation is equally applicable for imaging any source (not just point source) with arbitrary spatio-temporal characteristics.

We can model a distributed source as a succession of point sources that occur at locations $\boldsymbol{\xi}$, and with moment tensor $\mathbf{M}(\boldsymbol{\xi}, t)$ defined for $\mathbf{x} \in W$ and $t \in [0, T]$, and write

$$\mathbf{M}(\mathbf{x}, t) = \int \mathbf{M}(\boldsymbol{\xi}, t)\, \delta(\mathbf{x} - \boldsymbol{\xi})\, d\boldsymbol{\xi}\,. \tag{A1}$$

The n^{th} component of the data vector $\mathbf{d}(t)$ associated with the extended source and recorded by the station at $\mathbf{x}^i$ can be expressed as

$$d_n^i(t) = \int M_{pq}(\boldsymbol{\xi}, t) * \frac{\partial G_{np}(\mathbf{x}^i, t; \boldsymbol{\xi}, 0)}{\partial \xi_q}\, d\boldsymbol{\xi}, \tag{A2}$$

where $M_{pq}(\boldsymbol{\xi}, t)$ denotes the elements of the moment tensor $\mathbf{M}$ of the point source at $\boldsymbol{\xi}$, and G_{np} represents the elements of the elastodynamic Green tensor $\mathbf{G}$. In the frequency domain, equation A2 becomes

$$d_n^i(\omega) = \int M_{pq}(\boldsymbol{\xi}, \omega)\, \frac{\partial G_{np}(\mathbf{x}^i; \boldsymbol{\xi}, \omega)}{\partial \xi_q}\, d\boldsymbol{\xi}. \tag{A3}$$

The body force equivalent of the distributed source can be written as (Aki and Richards, 2002)

$$f_n(\mathbf{x}, t) = -\int M_{nq}(\boldsymbol{\xi}, t)\, \frac{\partial \delta(\mathbf{x} - \boldsymbol{\xi})}{\partial x_q}\, d\boldsymbol{\xi} \tag{A4}$$

where δ represents the Dirac delta function.

With A3 and A4 defining the data and the body force equivalent for the distributed source, we can repeat the same steps we took in section 2 to formulate the

optimization problem and obtain

$$a_p^j(\omega)\int_W G_{rn}^{i*}G_{rp}^j\,d\mathbf{x}=\int e^{i\omega T}M_{pq}^*\frac{\partial G_{np}^*(\mathbf{x}^i;\boldsymbol{\xi},\omega)}{\partial\xi_q}\,d\boldsymbol{\xi}, \tag{A5}$$

which can be simplified using A3 as

$$a_p^j(\omega)\int_W G_{rn}^{i*}\,G_{rp}^j\,d\mathbf{x}=e^{i\omega T}\,d_n^{i*}. \tag{A6}$$

Equation A6 represents a system of equations that can be concisely expressed as

$$\boldsymbol{\Gamma}(\omega)\,\mathbf{a}(\omega)=e^{i\omega T}\,\mathbf{d}^*(\omega), \tag{A7}$$

which has the exact form as equation 12 we obtained for a point source in section 2.

APPENDIX B: PARTICLE MOTION NEAR SOURCE

In section 2, we assumed that in the near-source region the particle displacements are proportional to the source equivalent force. Here, we justify this assumption by studying the behaviour of the particle displacements in the region near a unidirectional point force.

Consider an elastic medium with a point force $\mathbf{f}(t)$ applied at the origin. The displacement field $\mathbf{u}(\mathbf{x},t)$ due to this point force is (Aki and Richards, 2002)

$$\begin{aligned}u_i(\mathbf{x},t)=&\frac{1}{4\pi\rho}\,(3\gamma_i\gamma_j-\delta_{ij})\,\frac{1}{r^3}\int_{r/\alpha}^{r/\beta}\tau\,f_j(t-\tau)\,d\tau\\&+\frac{1}{4\pi\rho\alpha^2}\,\gamma_i\gamma_j\,\frac{1}{r}\,f_j(t-\frac{r}{\alpha})\\&-\frac{1}{4\pi\rho\beta^2}\,(\gamma_i\gamma_j-\delta_{ij})\,\frac{1}{r}\,f_j(t-\frac{r}{\beta}),\end{aligned} \tag{B1}$$

where $r=|\mathbf{x}|$ is the distance from the origin, $\gamma_i=x_i/r$ are the direction cosines, δ is the Dirac delta function, ρ is the density, α is the $P-$wave velocity, and β is the $S-$wave velocity with $\alpha>\beta$. Using B1, we can calculate the limit

$$\begin{aligned}\lim_{r\to0}4\pi\rho r\,u_i(\mathbf{x},t)=&\frac{1}{2}\,(\frac{1}{\alpha^2}+\frac{1}{\beta^2})\,\delta_{ij}\,f_j(t)\\&+\frac{1}{2}\,(\frac{1}{\beta^2}-\frac{1}{\alpha^2})\,\gamma_i\gamma_j\,f_j(t).\end{aligned} \tag{B2}$$

The expression on the right hand side of B2 is called the Somigliana tensor (Aki and Richards, 2002). In vector form, equation B2 is given by

$$\begin{aligned}\lim_{r\to0}4\pi\rho r\,\mathbf{u}(\mathbf{x},t)=&\frac{1}{2}\,(\frac{1}{\alpha^2}+\frac{1}{\beta^2})\,\mathbf{f}(t)\\&+\frac{1}{2}\,(\frac{1}{\beta^2}-\frac{1}{\alpha^2})\,\hat{\mathbf{r}}\,(\hat{\mathbf{r}}\cdot\mathbf{f}(t)),\end{aligned} \tag{B3}$$

where $\hat{\mathbf{r}}_i=\gamma_i$.

When $\hat{\mathbf{r}}\parallel\mathbf{f}$, expression B3 reduces to

$$\lim_{r\to0}4\pi\rho r\,\mathbf{u}(\mathbf{x},t)=\frac{1}{\beta^2}\,\mathbf{f}(t), \tag{B4}$$

and when $\hat{\mathbf{r}}\perp\mathbf{f}(t)$, expression B3 reduces to

$$\lim_{r\to0}4\pi\rho r\,\mathbf{u}(\mathbf{x},t)=\frac{1}{2}\,(\frac{1}{\alpha^2}+\frac{1}{\beta^2})\,\mathbf{f}(t). \tag{B5}$$

In both situations the displacement at the source location is parallel to the excitation. This result is confirmed by Wu and Ben-Menahem (1985) who show (Figure 2 of their paper) the motion of the elastodynamic field in the near-source region of a unidirectional force.